A Flexible, Adaptive, and Self-Powered Triboelectric Vibration Sensor with Conductive Sponge-Silicone for Machinery Condition Monitoring

Yongjiu Zou, Minzheng Sun, Xinyu Zhang, Junpeng Wang, Fangming Li, Fangyang Dong, Zhenhang Zhao, Taili Du,* Yulong Ji, Peiting Sun, and Minyi Xu*

Vibration sensors for continuous and reliable condition monitoring of mechanical equipment, especially detection points of curved surfaces, remain a great challenge and are highly desired. Herein, a highly flexible and adaptive triboelectric vibration sensor for high-fidelity and continuous monitoring of mechanical vibration conditions is proposed. The sensor is entirely composed of flexible materials. It consists of a conductive sponge-silicone layer and a fluorinated ethylene propylene film. It can detect vibration acceleration of 5 to 50 m s^{-2} and vibration frequency of 10 to 100 Hz. It has strong robustness and stability, and the output performance barely changes after the durability test of 168 000 working cycles. Additionally, the flexible sensor can work even when the detection point of the mechanical equipment is curved, and the linear fit of the output voltage and acceleration is very close to that when the detection point is flat. Finally, it can be applied to monitoring the working condition of blower and vehicle engine, and can transmit vibration signal to mobile phone application through Wi-Fi module for real-time monitoring. The flexible triboelectric vibration sensor is expected to provide a practical paradigm for smart, green, and sustainable wireless sensor system in the era of Internet of Things.

1. Introduction

With the rapid development of Internet of Things (IoT) and information/intelligent technology, wireless distributed sensor networks (WSNs) have been widely used in industry,[1] agriculture,[2] military,[3] and other fields.[4–6] Vibration sensors are widely used in machinery,[7] construction,[8] transportation,[9] and medical fields.[10] It can judge the operating condition of the equipment by monitoring the vibration parameters, such as frequency, amplitude, speed, and acceleration signals,[11–14] so as to improve the operating efficiency and safety. How to realize long-term reliable power supply of a large number of wireless vibration sensor nodes is one of the thorny problems.[15,16] Wireless vibration sensor nodes are now mostly powered by batteries, which have problems such as limited storage energy and need to be replaced regularly, limiting the use of wireless sensors, especially in places where sensors are urgently needed but power supply is difficult.[17,18] Therefore, as the power consumption of electronic devices becomes lower and lower, there is an urgent need to develop a sustainable, green, and universal alternative power supply solution.[19,20]

In 2012, Professor Wang Zhonglin's team invented the triboelectric nanogenerator (TENG), which is based on the principles of triboelectrification and electrostatic induction and has broad application prospects.[21–23] TENG has advantages of efficient mechanical-to-electrical energy conversion, self-sustainability, broad material availability, low cost, and good scalability, and can directly convert wide-band mechanical motion into high-voltage and low-noise electrical signals, presenting absolute advantages in the field of self-powered vibration sensing technology.[24–26] Recently, triboelectric vibration sensors have achieved more advanced results in the vibration monitoring of marine diesel engines,[27] blowers,[28] railway structures[29] and bridges.[30] According to the different structures, it is mainly divided into two categories: resonant vibration sensor[31,32] and non-resonant vibration sensor.[33,34] Resonant vibration sensors generally rely on the movement of assisted structures such as springs[35] and shrapnel[36] to generate electrical signals, but due to the constraints of assisted structures, its application in a wide range of vibration frequencies is limited. Non-resonant vibration sensors generally use small balls,[37,38] liquid metal,[39,40] mass blocks[8,41] as the internal structure of the device, through which electrical

Y. Zou, M. Sun, X. Zhang, J. Wang, F. Li, F. Dong, T. Du, M. Xu
Dalian Key Lab of Marine Micro/Nano Energy and Self-Powered Systems,
Marine Engineering College
Dalian Maritime University
Dalian 116026, China
E-mail: dutaili@dlmu.edu.cn; xuminyi@dlmu.edu.cn
Z. Zhao
Key Laboratory of Roads and Railway Engineering Safety Control
Ministry of Education
Shijiazhuang Tiedao University
Shijiazhuang 050043, China
Y. Ji, P. Sun
Marine Engineering College
Dalian Maritime University
Dalian 116026, China

**ADVANCED
SCIENCE NEWS**
www.advancedsciencenews.com

**NANO · MICRO
small**
www.small-journal.com

signals are generated with the movement of the vibration source. They detect amplitudes in the millimeter range, with a minimum of 3.5 μm, and frequencies ranging from 1 to 2000 Hz. However, the common problem they have now is that they can only detect the vibration condition when the measuring surface is a planar, and it is difficult to measure effectively when the measuring surface is a curved surface, such as industrial pipelines and equipment with special shape.[42,43] Therefore, designing highly flexible triboelectric vibration sensors capable of measuring curved surface vibration to improve the detection accuracy remains a major challenge.

Therefore, in this work, we report a highly flexible vibration sensor based on TENG (HF-TENG) for machinery condition monitoring. The HF-TENG consists of a conductive sponge-silicone layer and a fluorinated ethylene propylene (FEP) film attached to a flexible conductive fabric as the electrode. The sponge-silicone layer is formed by pouring silicone into a conductive sponge, where the silicone acts as the tribo-material and the conductive sponge acts as the electrode. The HF-TENG can detect vibration acceleration in the range of 5 to 50 m s^{-2} and vibration frequency in the range of 10 to 100 Hz. When the silicone mass is 2 g and the air gap is 1 mm, the output signal of the square HF-TENG is the strongest, and the linear fitting degree with the acceleration is the best. Meanwhile, the HF-TENG has strong robustness and stability, and the output performance barely changes after the durability test of 168 000 working cycles. Moreover, the output signal is processed by the designed circuit and transmitted to the Arduino Cloud mobile phone application (APP) through the Wi-Fi module to display the vibration parameters, which is successfully applied to the working condition monitoring of the blower and the vehicle engine. This work will greatly accelerate the development of wireless sensor networks and has important implications for providing sustainable energy solutions for smart sensing systems in the era of IoT.

2. Results and Discussion

2.1. Structure and Working Principle of the HF-TENG

As shown in **Figure 1a**, the application scenarios of HF-TENG are first demonstrated, including diesel engines, compressors, blowers, and other different types of mechanical equipment. Figure 1b further shows the structural design of HF-TENG. The HF-TENG is entirely composed of flexible materials. It consists of a conductive sponge-silicone layer and an FEP film with a layer of flexible conductive fabric attached to the back. A 0.5 mm thick conductive sponge as one electrode was infused with silicone, and the internal pores were filled with silicone, making the sponge-silicone layer very malleable (Figure 1c). The conductivity of conductive sponges has not yet reached the level of pure metals, but the gap between the two is not large, and it is feasible to use it as a conductor (Figure S1, Supporting Information). The bottom layer is a 0.1 mm thick layer of flexible conductive fabric that acts as another electrode (Figure 1d), on which is attached a 0.05 mm FEP film. To make the conductive sponge-silicone layer and FEP film fully contact and separate under the action of an external excitation source, a 1 mm wide rectangular silicone frame is added between them. At the same time, a cylindrical silicone mass is attached to the conductive sponge-silicone layer to increase the

intensity of the output signal by increasing the contact degree between the tribo-materials (The physical structure of the silicone mass and the fabrication procedure of the conductive sponge-silicone layer are shown in Figure S2, Supporting Information). Figure 1b,e,f shows the scanning electron microscope (SEM) images of the sponge-silicone layer and the flexible conductive fabric layer, respectively.

The working principle of HF-TENG is shown in Figure 1g. In the initial state, due to the external vibration excitation, the conductive sponge-silicone layer will bend down with the silicone mass and deform, and contact with the FEP film. Since the two tribo-materials, the conductive sponge-silicone layer and the FEP film, have different electronegativity, the silicone surface of the conductive sponge-silicone layer is positively charged when they come into contact, while the FEP is negatively charged. Then, the conductive sponge-silicone layer moves up and down periodically with the silicone mass, alternately contacting and separating the FEP, so that the electrons move back and forth between the two electrodes to balance the potential difference between them, thus forming an electric current. The potential distribution of HF-TENG during motion was simulated by COMSOL, which is completely consistent with the working principle (Figure 1h).

2.2. Theoretical Analysis

To systematically analyze the mechanical motion characteristics of HF-TENG, it is very important to find out the factors affecting its vibration motion law. Flexible vibration sensors are generally used to detect vibration information in the vertical direction of machinery. According to the structure of the sensor and the mechanical motion characteristics of the sponge-silicone layer, the vibration physical motion model of the sensor is simplified to the free vibration of the string, which will be more convenient and intuitive to explore the vibration system and obtain the factors affecting the vibration motion law. The coordinate system shown in **Figure 2a** is established for the x–axis with the connection of fixed points at both ends of the string. One of the segments dx is used for force analysis. The segment is subjected to the tension T' at the angle α' up and the tension T at the angle α down. It is important to note that in the absence of silicone mass, $T = \rho v^2 s$, where v is the wave velocity of the string, and s is the cross-sectional area of the string. When there is a silicone mass, the tension in the string is changed to $T = \rho v^2 s + \frac{mg}{l}$, where m is the mass of the silicone block, g is the acceleration due to gravity, and l is the length of the string. Additionally, there are inertial forces in the upward direction and gravitational forces acting downward in the vertical direction. Based on Newton's laws, we can formulate the equilibrium equation for forces in the vertical direction for the string as follows:[44]

$$T' \sin \alpha' - T \sin \alpha - P dx = \rho dx \frac{\partial u^2}{\partial t^2} \qquad (1)$$

u represents the vibration mode function of the string, ρ is the mass density of the string, P is an external force, and Y and γ is time.
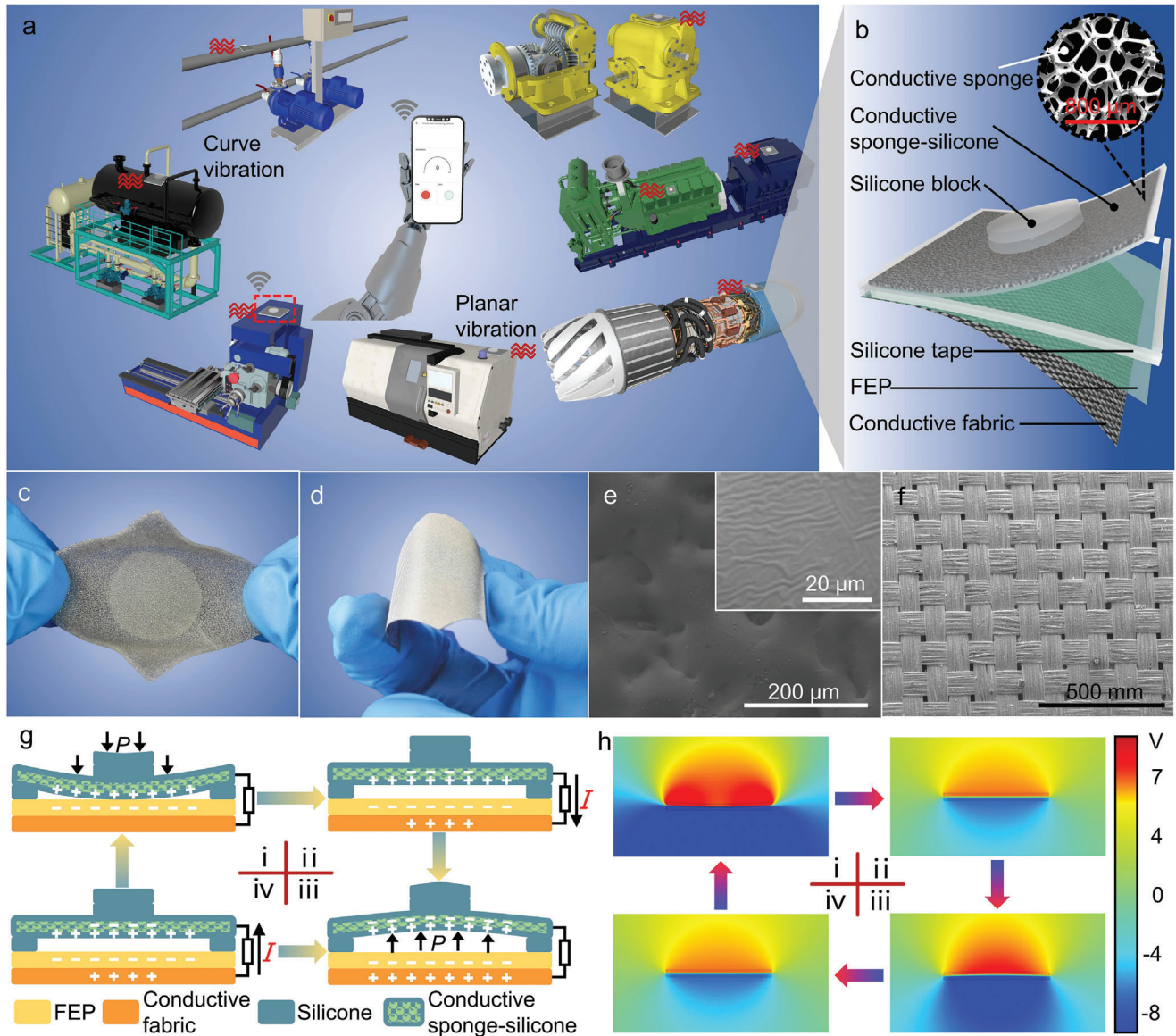
Figure 1. Application scenario, structure, and working principle of HF-TENG. a) Schematic diagram of the application scenarios of the HF-TENG. b) Structure of the highly flexible HF-TENG and SEM image of the conductive sponge. c) Tensile test diagram of the conductive sponge-silicone layer. d) Bending test diagram of conductive fabric. e) SEM image of the silicone surface of the conductive sponge-silicone layer. f) SEM images of surface of the conductive fabric. g) Working mechanism of the HF-TENG. h) COMSOL simulation of the periodic potential change between the two electrodes of the HF-TENG.

Due to the small vibration amplitude, angles α and α' are ≈ 0; we can derive the following equations:

$$\sin \alpha = \tan \alpha = \frac{\partial u(x, \gamma)}{\partial x} \tag{2}$$

$$\sin \alpha' = \tan \alpha' = \frac{\partial u(x + \mathrm{d}x, \gamma)}{\partial x} \tag{3}$$

$$\frac{\partial u(x + \mathrm{d}x, \gamma)}{\partial x} - \frac{\partial u(x, \gamma)}{\partial x} = \frac{\partial u^2(x, \gamma)}{\partial x^2} \mathrm{d}x \tag{4}$$

Substituting Equations (2), (3), and (4) into Equation (1):

$$T\left[\frac{\partial u^2(x, \gamma)}{\partial x^2}\right] = P(x, \gamma) + \rho \frac{\partial u^2(x, \gamma)}{\partial t^2} \tag{5}$$

To further solve Equation (5) using the method of separation of variables, let's assume $u(x, \gamma) = X(x) \times Y(\gamma)$, $a^2 = \frac{T}{\rho}$, x is the distance from $\mathrm{d}x$ to the origin, $X(x)$ is the displacement component, and $Y(\gamma)$ is the time component. Considering the free vibration of the structure, as follows:

$$a^2 X''(x) \times Y(\gamma) = X(x) \times Y''(\gamma) \tag{6}$$

**ADVANCED
SCIENCE NEWS**

www.advancedsciencenews.com

**NANO · MICRO
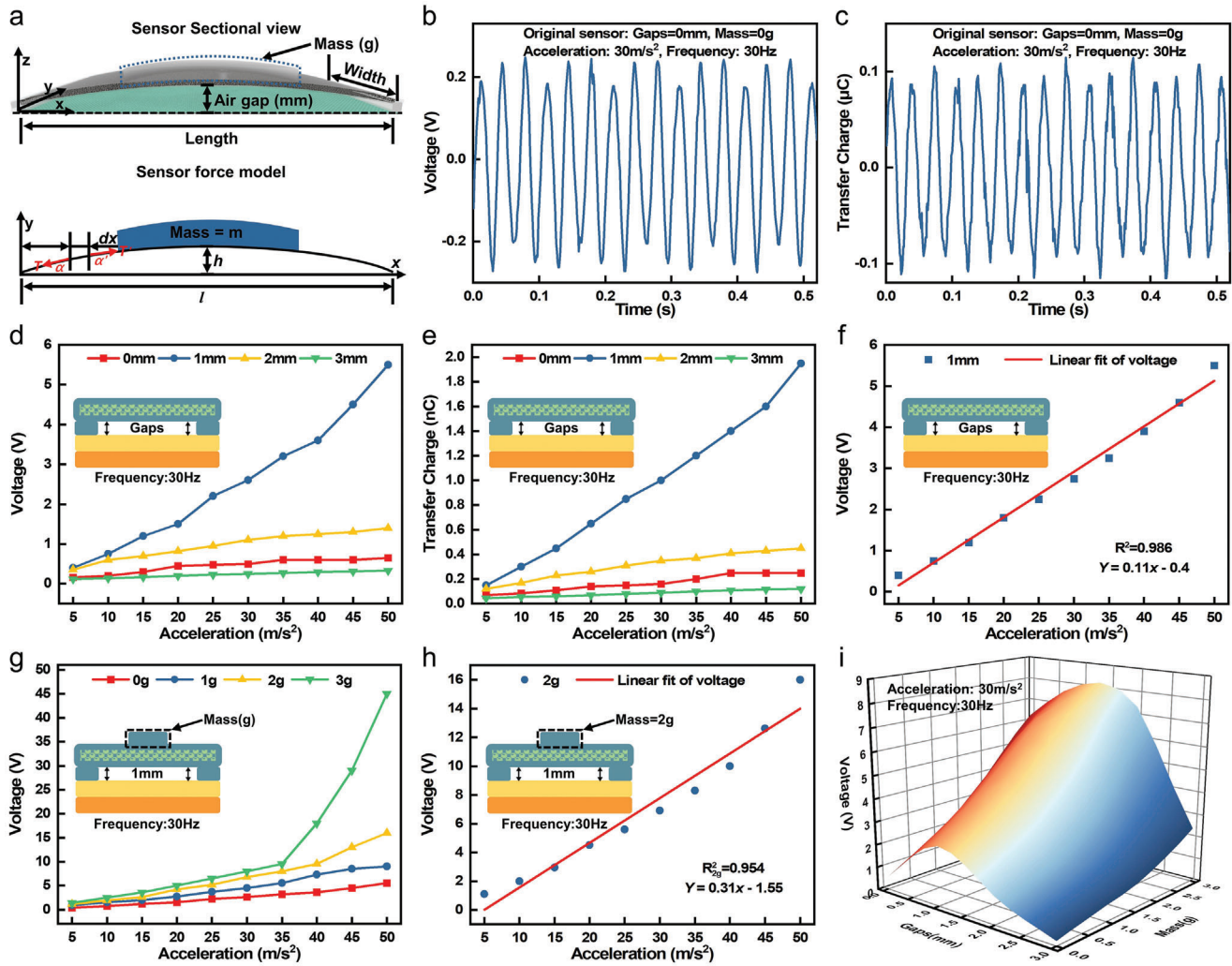small**

www.small-journal.com

Figure 2. Kinematic characteristics and output performance of the HF-TENG. a) The theoretical model of the HF-TENG. b) The open-circuit voltage and c) transferred charge of the original flexible sensor at 30 Hz frequency and 30 m s^{-2} acceleration. d) Open-circuit voltage and e) transferred charge with different air gaps under the accelerations of 5–50 m s^{-2} when the frequency is 30 Hz. f) Linear relationship between the open-circuit voltage and acceleration at the frequency of 30 Hz when the air gap is 1 mm. g) Open-circuit voltage of various silicone mass at frequency of 30 Hz under different accelerations. h) Linear relationship between the open-circuit voltage and acceleration at the frequency of 30 Hz when the silicone mass is 2 g. i) A 3D graph of the open-circuit voltage at the frequency of 30 Hz with different air gaps and silicone mass.

Introduce the constant $-\omega^2$ into Equation (6) as follows:

$$a^2 X''(x) \times Y(y) = -\omega^2$$
$$X(x) \times Y''(y) = -\omega^2 \qquad (7)$$

Utilize the general solution method based on differential equations; we obtain the final Equation (8) as follows:

$$X = A\cos\left(\frac{\omega}{a}x\right) + B\sin\left(\frac{\omega}{a}x\right)$$
$$Y = C\cos(\omega y) + D\sin(\omega y) \qquad (8)$$

Under the circumstances, A and B are linked to the boundary conditions of the string, $X(0) = X(l) = 0$, C and D are associated with the initial conditions of the string. Additionally, $\omega = \frac{i\pi}{l}$, $i = $

$0, 1, 2, \ldots$ and $a = \sqrt{\frac{T}{\rho}}$ have significant effects on the vibrational mode functions of the string.

In conclusion, according to the initial conditions and boundary conditions, the mechanical motion state of the structure can be obtained. At the same time, according to the motion state of the shaker, the relative displacement between the tribo-materials can be obtained. When the relative displacement is greater than or equal to air gap, the upper and lower tribo-materials contact alternately to generate current.

2.3. Electrical Output Performance of HF-TENG

To systematically investigate the output performance of the HF-TENG, the main parameters to be considered include weight mass, air clearance, and shape. The concentration of metallic

**ADVANCED
SCIENCE NEWS**

www.advancedsciencenews.com

**NANO · MICRO
small**

www.small-journal.com

ingredients in conductive sponges should also affect the output performance, but the laboratory does not have the conditions for processing and production at present, we purchased the finished products, and the manufacturer can only provide products with this concentration, so we did not explore this aspect later, but it will become our future research topic. An experimental platform (shown in Figure S3, Supporting Information) was built to test the working performance of the HF-TENG. Figure 2b and c respectively show the output voltage and transferred charge of the original HF-TENG in square shape (without silicone mass and with no air gap), and the current signals are shown in Figure S4, Supporting Information. When the vibration acceleration is 30 m s^{-2} and the frequency is 30 Hz, the output signal is relatively stable but not strong enough. To enhance the strength of output signal, the method of increasing the silicone mass and air gap is adopted. Since the selected research object works at a fixed frequency of 30 Hz, the vibration frequency is controlled at 30 Hz when studying the influence of air gap. First, in the absence of the silicone mass, Figure 2d shows the variation of output voltage with acceleration at different air gaps when the vibration frequency is 30 Hz. The output voltage is significantly improved compared with the original device, and it increases with the increase of acceleration. When the air gap is 1 mm, the output performance is the best, and the changes in other conditions are relatively not particularly obvious. The amount of transferred charge shown in Figure 2e also exhibits the same variation characteristics (signals for short-circuit current are shown in Figure S5, Supporting Information). Figure 2f shows the linear fitting diagram when the air gap is 1 mm, showing a better effect. Then, the influence of the different silicone masses on the output performance is explored when the air gap is 1 mm. Figure 2g shows how the output voltage of different silicone masses varies with the acceleration when the vibration frequency is 30 Hz (the short-circuit current and transferred charge are shown in Figure S6, Supporting Information). It can be clearly seen that the output voltage has further increased, and it also increases with the increase of acceleration. When the silicone mass is 3 g, the output voltage is the largest, but when the acceleration is greater than 35 m s^{-2}, the output voltage suddenly becomes large, and the overall linearity is not good. On the contrary, when the silicone mass is 2 g, although the output voltage is not the maximum, it also increases linearly with the increase of acceleration (Figure 2h). Therefore, for the following experimental exploration, devices are selected to match with the best output effect, that is, the air gap is 1 mm and the silicone mass is 2 g (the linear fitting of other air gaps and silicone mass as shown in Figure S7, Supporting Information). Figure 2i and Figure S8, Supporting Information sterically show the variation of output performance of HF-TENG with air gap and silicone mass when the acceleration is 30 m s^{-2} and the frequency is 30 Hz.

Furthermore, the influence of different shapes of sensor (square, triangle, and circle) on the output performance is also explored (**Figure 3**a). Figure 3b,c shows the variation of output voltage of triangular and circular sensors with vibration acceleration, respectively (signals of short-circuit current and transferred charge are shown in Figure S9, Supporting Information). It can be clearly seen that the output voltage change of the triangle sensor is too stable and the differentiation is small. However, the output voltage of the circular sensor has a sudden change

when the acceleration is greater than 35 m s^{-2}, and the performance tends to remain unchanged as the acceleration continues to increase. Figure 3d clearly compares the linearity of the output performance of the three sensors with different shapes. It can be seen that the output signal of the square sensor has the largest intensity and the highest linearity (Detailed output performance is compared in Figure S10, Supporting Information). Next, we continue to study the influence of vibration frequency on the output performance of HF-TENG. Figure 3e,f and Figure S11, Supporting Information respectively show the vibration of the output voltage, transferred charge and short-circuit current of the square sensor with acceleration at different frequencies, all of which show a good linear relationship (Figure S12, Supporting Information). As can be seen from Figure 3g, when the amplitude is 0.5 mm, the voltage of square sensor increases with the increase of frequency, showing a good linearity (Figure 3h). At the same time, the amount of transferred charge and short-circuit current of the square sensor also present a good linear relationship under the same condition (Figure 3i and Figure S13, Supporting Information). Finally, the durability experiment of the sensor is done. After about 168 000 working cycles, the output effect is almost unchanged, proving that it can work for a long time (Figure 3j).

Since in the actual mechanical application scenario, not all the working surfaces are planar, there are many curved surfaces.[45,46] Therefore, to demonstrate the advantages that HF-TENG can also work normally and effectively on curved working surface, experiments are conducted to measure vibration information with a flexible sensor on a curved pipe, and the output performance measured by the sensor on a planar surface is compared. **Figure 4**a shows the simulation platform for HF-TENG testing on a bend pipe. Figure 4b and c respectively show that when the inner diameter of the bending pipe is 10 cm, both the output voltage and the amount of transferred charge of the HF-TENG increase linearly with the increase of vibration acceleration (signals of short-circuit current is shown in Figure S14, Supporting Information). Under the same condition, different inner diameters of bending pipe are also investigated experimentally. Figure 4d shows the variation law of output voltage and acceleration when the inner diameter of the bending pipe is 5,10,15 cm, both of which show good linearity. Moreover, when the acceleration is 30 m s^{-2}, the output voltage generated by the experiments on the curved surface is slightly lower than that on the planar surface under the same condition (Figure 4e). Signals of short-circuit current and transferred charge are shown in Figure S15, Supporting Information. In the same case, the transfer charge and short-circuit current also show a good linear relationship with acceleration (Figure 4f and Figure S16, Supporting Information). Furthermore, Figure 4g shows the comparison of linear fit between the output voltage and acceleration measured on a planar and a curved surface, indicating that the proposed HF-TENG has the same good linearity measured on a curved tube as that measured on a planar table, except that the strength of the output signal is slightly reduced (Figure S17, Supporting Information). Then the variation law of output voltage with frequency under the bending environment is carried out. As can be seen from Figure 4h, when the vibration amplitude is 0.5 mm, the output voltage increases with the increase of frequency, and a better linear fit is demonstrated (Figure 4i). At different frequencies, the
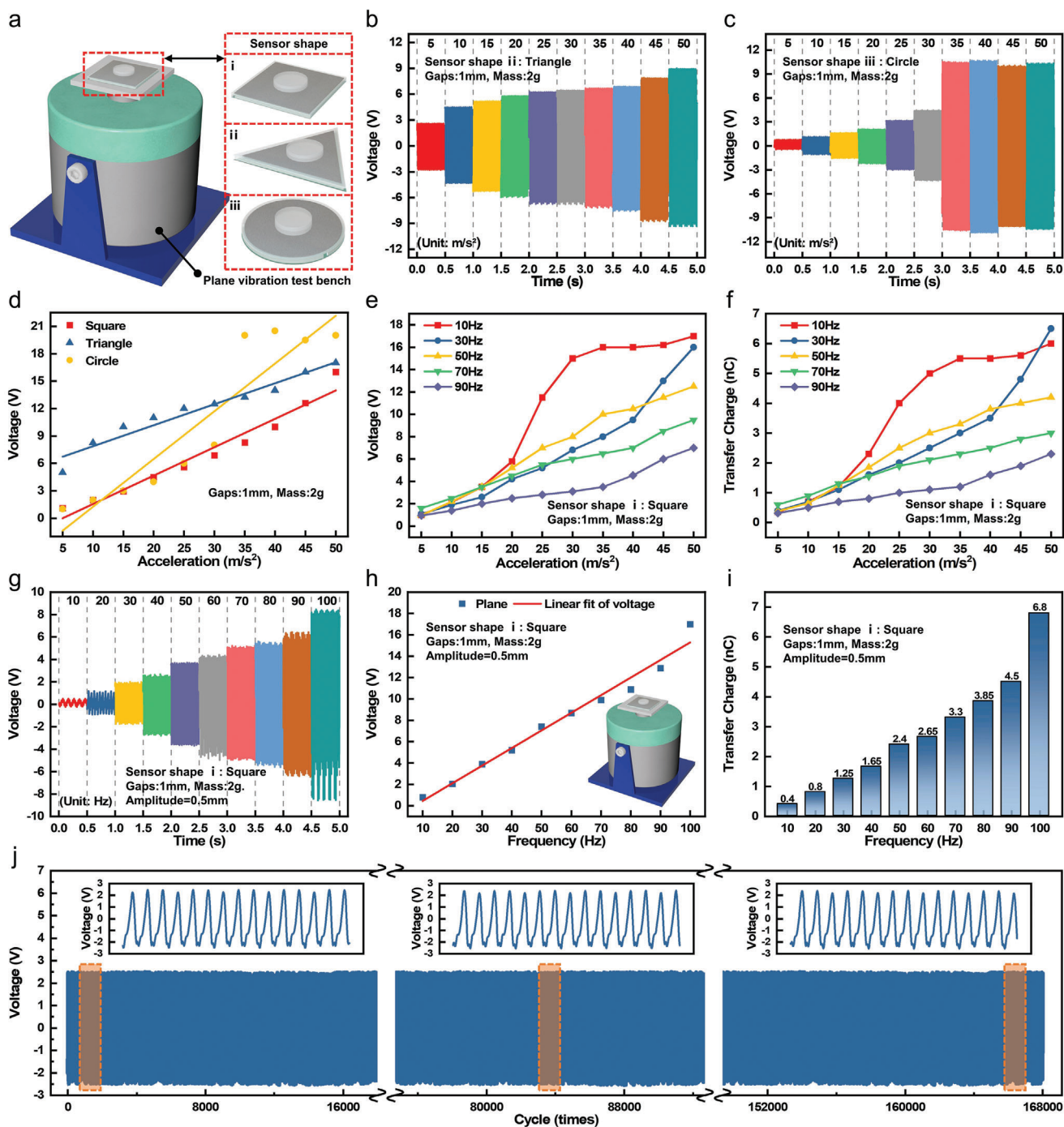
**ADVANCED
SCIENCE NEWS**

www.advancedsciencenews.com

**NANO · MICRO
small**

www.small-journal.com

Figure 3. Effect of sensor shape and vibration frequency on the output performance of HF-TENG. a) Schematic diagram of the experiment device and different shapes of the HF-TENG. Open-circuit voltage of b) triangular and c) circular HF-TENGs at the frequency of 30 Hz and different accelerations. d) Linear relationship between the open-circuit voltage and acceleration at different shapes when the frequency is 30 Hz. e) Open-circuit voltage and f) transferred charge of HF-TENG at different accelerations when the frequency is 10–90 Hz. g) Open-circuit voltage and i) transferred charge with different vibration frequencies under fixed vibration amplitude of 0.5 mm. h) Linear relationship between the open-circuit voltage and vibration frequency at different frequencies under fixed vibration amplitude of 0.5 mm. j) Electrical output stability of the HF-TENG.
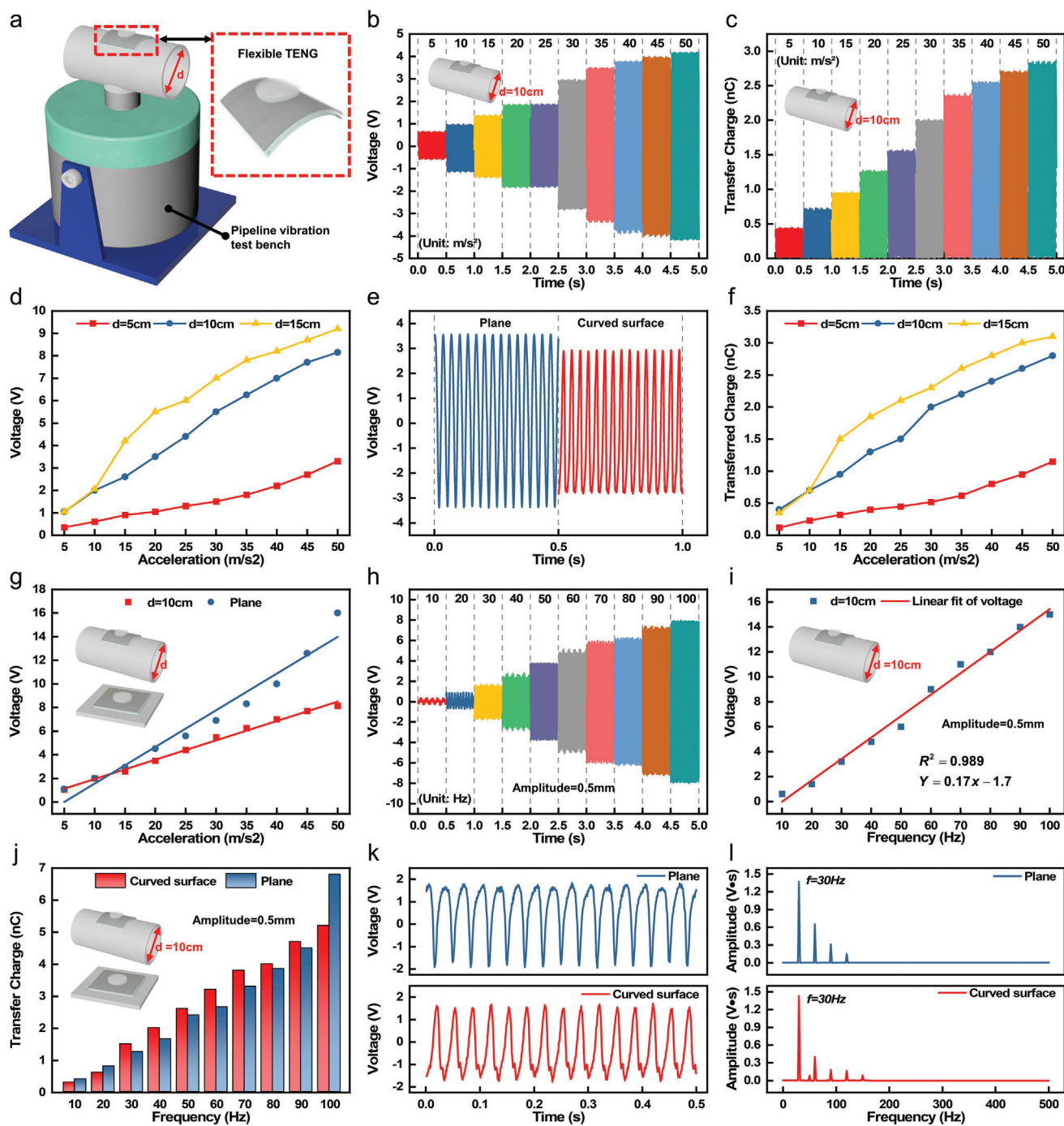
ADVANCED
SCIENCE NEWS

www.advancedsciencenews.com

NANO · MICRO
small
www.small-journal.com

Figure 4. The output performance of HF-TENG on a curved surface. a) Schematic diagram of a curved shaker. b) Open-circuit voltage and c) transferred charge of HF-TENG at the frequency of 30 Hz with different accelerations on a curved shaking table. The d) open-circuit voltage and f) transferred charge of HF-TENG at different accelerations on a curved vibration table with different diameters when the frequency is 30 Hz. e) Comparison of the output voltage signals of HF-TENG on planar and curved shaking tables at frequency of 30 Hz and acceleration of 30 m s^{-2}. g) The linear relationship between open-circuit voltage and acceleration at the frequency of 30 Hz on the planar and curved vibration table. h) Open-circuit voltage of HF-TENG with different vibration frequencies at a fixed amplitude of 0.5 mm on a curved vibration table. i) Linear relationship between the open-circuit voltage and vibration frequency on a curved vibration table when the vibration amplitude is 0.5 mm. j) Comparison of transferred charges at different vibration frequencies at an amplitude of 0.5 mm on flat and curved vibration tables. k) Comparison of open-circuit voltage at the frequency of 30 Hz and amplitude of 0.5 mm on planar and curved vibration tables. l) Frequency domain obtained by Fourier transform of the voltage signals in k).
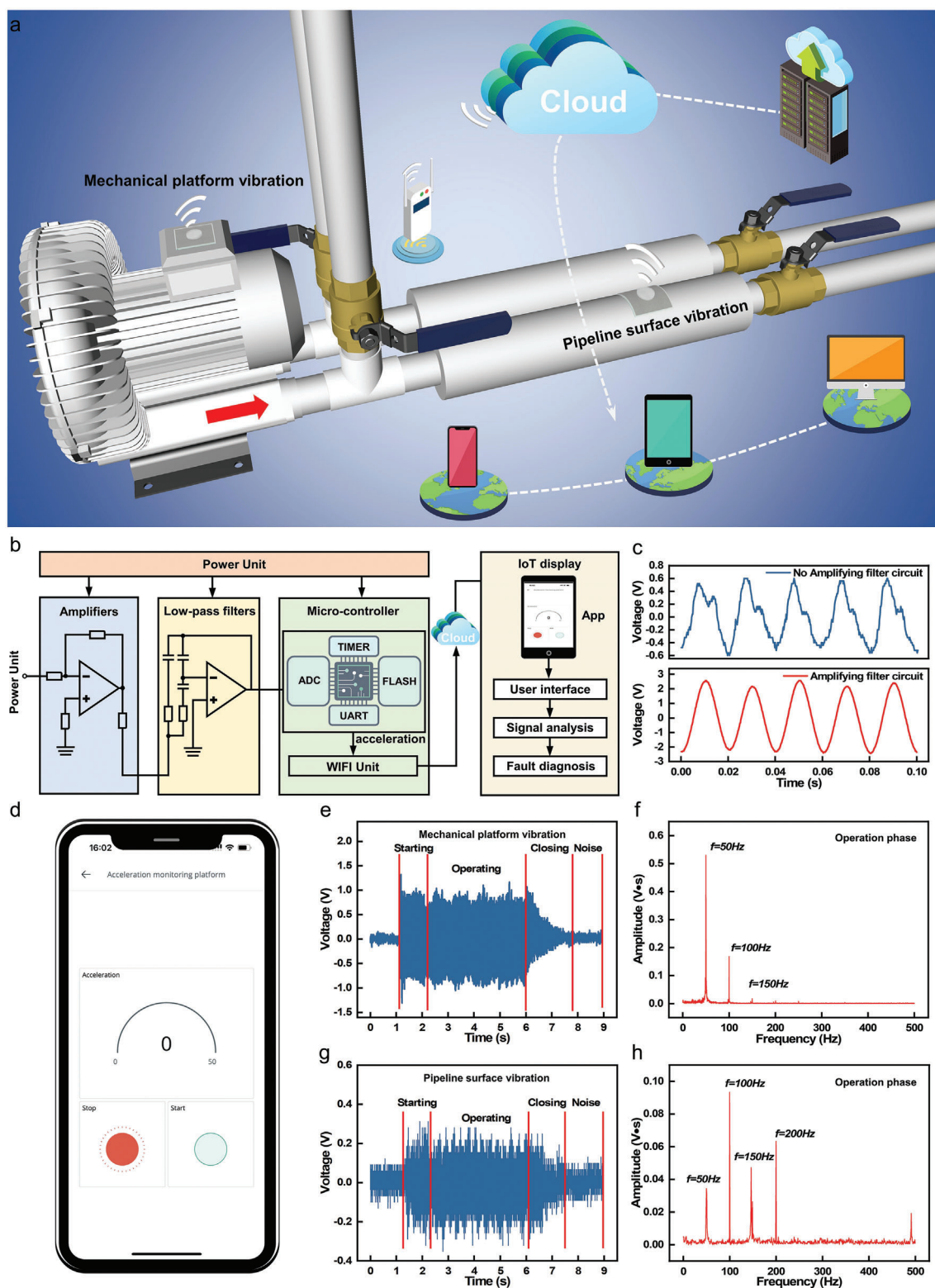
Figure 5. Application of HF-TENG sensor in machinery vibration monitoring. a) Schematic diagram of test platform for HF-TENG. b) A schematic diagram of the flexible triboelectric sensor-based vibration signal management circuit composed of data acquisition, signal processing, wireless transmission, and signal display. c) Comparison of output voltage signals using and not using the proposed circuits. d) A visualization platform for real-time vibration monitoring using mobile phone APP. Outputs voltage signals of HF-TENG during operation of e) blower and g) pipeline. Fourier Transform of voltage signal during operation of f) blower and h) pipeline.

**ADVANCED
SCIENCE NEWS**

www.advancedsciencenews.com

NANO · MICRO

small

www.small-journal.com

amount of transferred charge measured on the curved tube is almost the same as that measured on the planar surface (Figure 4j). The signals of output current are shown in Figure S18, Supporting Information. And when the frequency is 30 Hz, the output voltage generated by the experiments on the curved tube is almost equal to the result on the planar surface under the same condition (Figure 4k). Finally, Fourier transform is performed on both the output voltage measured on the planar and the curved surface as mentioned in Figure 4k, and the spectrum diagram of the two scenarios is obtained (Figure 4l). The transferred charge and Fourier transform of the output voltage of HF-TENG at the frequency of 10–100 Hz are shown in Figures S19 and S20, Supporting Information. It can be clearly seen that the spectrum diagram of the electrical signal obtained by the proposed flexible sensor is completely consistent with the vibration frequency of the exciter.

To demonstrate the practical application effect, a vibration monitoring platform is built, as shown in **Figure 5a**. Both planar and curved surface vibration can be tested on this platform, and the data can be sent to the cloud server in real time. In addition, a demonstration of the HF-TENG on both planar and curved surfaces can be seen in Movies S1 and S2, Supporting Information. To improve user-friendliness, we built a platform that can process and display the measured vibration signals in real time, consisting of a flexible sensor, signal processing circuit, Wi-Fi module, and the Arduino Cloud mobile phone APP. Figure 5b shows in detail the complete process flow chart of the vibration signal from acquisition to display on the screen of the mobile phone, including software and hardware. As can be seen from Figure 5c, the output signal will be smoother after adopting the designed circuit, and the output clutter of the signal will be reduced. Figure 5d is the visual interface of the designed mobile phone APP, which can display information such as vibration acceleration and frequency in real time. Finally, the practical application scenarios of planar and curved surfaces are tested. First, on the planar surface, we placed the flexible sensor on the blower (Movie S3, Supporting Information), and obtained the signal curve of the blower start–run–stop condition (Figure 5e). At the same time, Fourier transform spectrum analysis was performed for the signals at different stages of start-run-stop condition (Figure 5f and Figure S21, Supporting Information). The flexible vibration sensor not only detects the main frequency signal of 50 Hz, but also effectively detects the harmonic signal of 100 Hz and 150 Hz, which is usually used as one of the indicators to detect some mechanical failure of the machinery. Then, on the curved surface, we placed the flexible sensor on the exhaust pipe of the blower (Movie S4, Supporting Information), and obtained the vibration signal from the exhaust pipe during the start–run–stop of the blower (Figure 5g). Meanwhile, Fourier transform spectrum analysis was performed for the signals at different stages of start–run–stop condition of the blower (Figure 5h and Figure S22, Supporting Information). The voltage signal diagram and spectrum diagram are obviously different from the results measured on the planar surface of the air compressor. The vibration signals detected on the curved surface are all harmonic signals because they are far away from the vibration source. Finally, we also tested the vibration of the car engine and showed a good measurement effect (Figure S23 and Movie S5, Supporting Information).

3. Conclusions

In summary, we proposed a highly flexible self-powered triboelectric vibration sensor for machinery condition monitoring, especially when the measuring point is a curved surface. The HF-TENG consists of a conductive sponge-silicone layer and an FEP film attached to a flexible conductive fabric as the electrode. The HF-TENG can detect vibration acceleration in the range of 5 to 50 m s^{-2} and vibration frequency in the range of 10 to 100 Hz. When the shape of HF-TENG is square, the silicone mass is 2 g, and the air gap is 1 mm, the intensity of the output signal is the largest. At an acceleration of 30 m s^{-2}, the open-circuit voltage and transfer charge, respectively, reach up to 7 V and 2.5 nC, and the linear fit with the acceleration is the best, among them, the plane is 0.954 and the surface is 0.989, indicating high stability under even under curved surfaces. Meanwhile, the HF-TENG has strong robustness and stability, and the output performance barely changes after the durability test of 168 000 working cycles. Further, the output signal is processed by the designed circuit and transmitted to the Arduino Cloud mobile phone APP through the Wi-Fi module to display the vibration parameters, which is successfully applied to the working condition monitoring of the blower and the vehicle engine. Above all, the developed highly flexible triboelectric vibration sensor is a solid step toward WSNs in the era of IoT.

4. Experimental Section

Fabrication of the HF-TENG: The HF-TENG consists of a conductive sponge-silicone layer and an FEP film. The sponge-silicone layer was formed by pouring silicone into a square conductive sponge with a side length of 400 mm and a thickness of 0.5 mm, where the silicone acts as the tribo-material and the conductive sponge acts as the electrode. The conductive sponge-silicone layer has good flexibility and ductility. The FEP film was a square shape with a side length of 400 mm and a thickness of 0.05 mm. A layer of flexible conductive fabric of 0.1 mm was attached to the lower surface as another electrode. To keep a certain distance between the conductive sponge-silicone layer and the FEP film, a 2 mm wide rectangular silicone frame with thicknesses of 1, 2, and 3 mm was added between them and then a 2 mm wide hole was cut in each corner of the rectangular frame for discharging air. At the same time, the conductive sponge-silicone layer was bonded to the above cylindrical silicone mass block, with the mass of 1, 2, and 3 g.

Electrical Measurement: The HF-TENG was mounted on an electrodynamic shaker (JZK-20) and was driven by amplified sine waves from a function generator (YE1311) and then an amplifier (YE5852). The acceleration was measured by a commercial accelerometer (KS96.100) and displayed in DASP software (Inelta, Chengdu, China). The electric output signals, including open-circuit voltage, short-circuit current, and transferred charge, were measured by an electrometer (Keithley 6514). For the vibration acceleration sensing test platform in Figure 5, the output signal of HF-TENG was transmitted to the designed circuit, the acquired signal was amplified by signal amplifier (AD620), and interference signal and ambient noise were eliminated by low-pass filter (UAF42). A microcontroller (Arduino MKR WiFi 1010) unit was used to convert the filtered analog signal into digital signal, and then convert it into real-time mechanical vibration acceleration after processing and analysis. Finally, rely on the Wi-Fi module of Arduino MKR WiFi 1010 to transmit the acceleration value to terminal applications such as mobile phones or computers.

Supporting Information

Supporting Information is available from the Wiley Online Library or from the author.

Acknowledgements

Conflict of Interest

The authors declare no conflict of interest.

Data Availability Statement

The data that support the findings of this study are available from the corresponding author upon reasonable request.

Keywords

[1] H. Bai, S. Li, J. Barreiros, Y. Tu, C. R. Pollock, R. F. Shepherd, *Science* **2020**, *370*, 848.

[2] T. Zhou, P. Zhang, Z. Yu, M. Tao, D. Zhou, B. Yang, T. Zhang, *Nano Energy* **2023**, *108*, 108216.

[3] A. M. Aziz, *Aktuel. Aspekte Kernfusionsforsch., Informationstag.* **2014**, *18*, 175.

[4] H. Wu, Z. Wang, B. Zhu, H. Wang, C. Lu, M. Kang, S. Kang, W. Ding, L. Yang, R. Liao, J. Wang, Z. L. Wang, *Adv. Energy Mater.* **2023**, *13*, 2300051.

[5] D. Liu, C. Li, P. Chen, X. Zhao, W. Tang, Z. L. Wang, *Adv. Energy Mater.* **2022**, *13*, 2202691.

[6] J. Li, T. Kim, N. Lapusta, E. Biondi, Z. Zhan, *Nature* **2023**, *620*, 800.

[7] H. Zhao, M. Shu, Z. Ai, Z. Lou, K. W. Sou, C. Lu, Y. Jin, Z. Wang, J. Wang, C. Wu, Y. Cao, X. Xu, W. Ding, *Adv. Energy Mater.* **2022**, *12*, 2201132.

[8] H. Wu, J. Wang, Z. Wu, S. Kang, X. Wei, H. Wang, H. Luo, L. Yang, R. Liao, Z. L. Wang, *Adv. Energy Mater.* **2022**, *12*, 2103654.

[9] L. Zhu, Z. Zhang, D. Kong, C. Liu, Z. Cao, W. Chen, C. Zhang, *Nano Energy* **2022**, *97*, 107165.

[10] J. H. Lee, K. H. Cho, K. Cho, *Adv. Mater.* **2023**, *35*, 2209673.

[11] Y. Chen, Y.-C. Wang, Y. Zhang, H. Zou, Z. Lin, G. Zhang, C. Zou, Z. L. Wang, *Adv. Energy Mater.* **2018**, *8*, 1802159.

[12] S. Wang, S. Niu, J. Yang, L. Lin, Z. L. Wang, *ACS Nano* **2014**, *8*, 12004.

[13] X. Gao, M. Huang, G. Zou, X. Li, Y. Wang, *Nano Energy* **2023**, *111*, 108356.

[14] M. Xu, P. Wang, Y. C. Wang, S. L. Zhang, A. C. Wang, C. Zhang, Z. Wang, X. Pan, Z. L. Wang, *Adv. Energy Mater.* **2017**, *8*, 1702432.

[15] H. Yu, N. Li, N. Zhao, *Adv. Energy Mater.* **2020**, *11*, 2002646.

[16] C. S. Wu, A. C. Wang, W. B. Ding, H. Y. Guo, Z. L. Wang, *Adv. Energy Mater.* **2019**, *9*, 1802906.

[17] F. Wang, M. Zhou, P. Wu, L. Gao, X. Chen, X. Mu, *Nano Energy* **2023**, *114*, 108662.

[18] Y. Zi, J. Wang, S. Wang, S. Li, Z. Wen, H. Guo, Z. L. Wang, *Nat. Commun.* **2016**, *7*, 10987.

[19] Y. Jia, Q. Jiang, H. Sun, P. Liu, D. Hu, Y. Pei, W. Liu, X. Crispin, S. Fabiano, Y. Ma, Y. Cao, *Adv. Mater.* **2021**, *33*, 2102990.

[20] A. M. Abdullah, A. Flores, A. R. Chowdhury, J. Li, Y. Mao, M. J. Uddin, *Nano Energy* **2020**, *73*, 104774.

[21] H. Zhao, M. Xu, M. Shu, J. An, W. Ding, X. Liu, S. Wang, C. Zhao, H. Yu, H. Wang, C. Wang, X. Fu, X. Pan, G. Xie, Z. L. Wang, *Nat. Commun.* **2022**, *13*, 3325.

[22] Z. Tang, S. Lin, Z. L. Wang, *Adv. Mater.* **2021**, *33*, 2102886.

[23] C. Wu, W. Ding, R. Liu, J. Wang, A. C. Wang, J. Wang, S. Li, Y. Zi, Z. L. Wang, *Mater. Today* **2018**, *21*, 216.

[24] S. Li, D. Liu, Z. Zhao, L. Zhou, X. Yin, X. Li, Y. Gao, C. Zhang, Q. Zhang, J. Wang, Z. L. Wang, *ACS Nano* **2020**, *14*, 2475.

[25] W. Song, B. Gan, T. Jiang, Y. Zhang, A. Yu, H. Yuan, N. Chen, C. Sun, Z. L. Wang, *ACS Nano* **2016**, *10*, 8097.

[26] H. Yu, Z. Xi, Y. Zhang, R. Xu, C. Zhao, Y. Wang, X. Guo, Y. Huang, J. Mi, Y. Lin, T. Du, M. Xu, *Nano Energy* **2023**, *107*, 108182.

[27] S. Hu, T. Han, Y. Qi, C. Zhang, X. Shi, Z. Peng, *Nano Energy* **2023**, *109*, 108308.

[28] C. Wang, X. Zhang, J. Wu, X. Yu, T. Cheng, H. Ma, Z. L. Wang, *Mech. Syst. Signal Process.* **2022**, *166*, 108429.

[29] X. J. Zhao, G. W. Wei, X. H. Li, Y. Qin, D. D. Xu, W. Tang, H. J. Yin, X. K. Wei, L. M. Jia, *Nano Energy* **2017**, *34*, 549.

[30] K. Xia, J. Liu, W. Li, P. Jiao, Z. He, Y. Wei, F. Qu, Z. Xu, L. Wang, X. Ren, B. Wu, Y. Hong, *Nano Energy* **2023**, *105*, 107974.

[31] J. Chen, G. Zhu, W. Q. Yang, Q. S. Jing, P. Bai, Y. Yang, T. C. Hou, Z. L. Wang, *Adv. Mater.* **2013**, *25*, 6094.

[32] A. Yu, P. Jiang, Z. L. Wang, *Nano Energy* **2012**, *1*, 418.

[33] M. T. Rahman, S. M. S. Rana, M. Salauddin, P. Maharjan, T. Bhatta, H. Kim, H. Cho, J. Y. Park, *Appl. Energy* **2020**, *279*, 115799.

[34] K. Xia, J. Fu, Z. Xu, *Adv. Energy Mater.* **2020**, *10*, 2000426.

[35] I. Mehamud, P. Marklund, M. Björling, Y. Shi, *Nano Energy* **2022**, *98*, 107292.

[36] Z. Ren, L. Wu, J. Zhang, Y. Wang, Y. Wang, Q. Li, F. Wang, X. Liang, R. Yang, *ACS Appl. Mater. Interfaces* **2022**, *14*, 5497.

[37] V. Vivekananthan, A. Chandrasekhar, N. R. Alluri, Y. Purusothaman, G. Khandelwal, R. Pandey, S.-J. Kim, *Nano Energy* **2019**, *64*, 103926.

[38] X. Xiao, X. Zhang, S. Wang, H. Ouyang, P. Chen, L. Song, H. Yuan, Y. Ji, P. Wang, Z. Li, M. Xu, Z. L. Wang, *Adv. Energy Mater.* **2019**, *9*, 1902460.

[39] B. Zhang, L. Zhang, W. Deng, L. Jin, F. Chun, H. Pan, B. Gu, H. Zhang, Z. Lv, W. Yang, Z. L. Wang, *ACS Nano* **2017**, *11*, 7440.

[40] J. Park, I. Kim, J. Yun, D. Kim, *Nano Energy* **2021**, *89*, 106442.

[41] P. S. Rui, W. Zhang, Y. M. Zhong, X. X. Wei, Y. C. Guo, S. W. Shi, Y. L. Liao, J. Cheng, P. H. Wang, *Nano Energy* **2020**, *74*, 104937.

[42] S. He, Z. Wang, X. Zhang, Z. Yuan, Y. Sun, T. Cheng, Z. L. Wang, *ACS Appl. Mater. Interfaces* **2022**, *14*, 2825.

[43] H. Zhang, Y. Yang, Y. Su, J. Chen, K. Adams, S. Lee, C. Hu, Z. L. Wang, *Adv. Funct. Mater.* **2014**, *24*, 1401.

[44] R. Gao, D. A. Ralescu, *IEEE Transactions on Fuzzy Systems*, Vol. *27*, IEEE, Piscataway, NJ **2018**, pp. 1323–1331.

[45] Y. Jia, K. Zhang, *Nano Energy* **2022**, *96*, 107103.

[46] H.-T. Deng, X.-R. Zhang, Z.-Y. Wang, D.-L. Wen, Y.-Y. Ba, B. Kim, M.-D. Han, H.-X. Zhang, X.-S. Zhang, *Nano Energy* **2021**, *83*, 105823.